Title

Bladder surface dose modeling in prostate cancer radiotherapy: An analysis of motion-induced variations and the cumulative dose across the treatment

Journal

Medical Physics, 48(12)

ISSN

0094-2405

Authors

Lao, Yi
Cao, Minsong
Yang, Yingli
et al.

Publication Date

2021-12-01

DOI

10.1002/mp.15326

Peer reviewed

HHS Public Access

Author manuscript

Med Phys. Author manuscript; available in PMC 2022 December 01.

Published in final edited form as:

Med Phys. 2021 December ; 48(12): 8024–8036. doi:10.1002/mp.15326.

Bladder surface dose modeling in prostate cancer radiotherapy: an analysis of motion-induced variations and the cumulative dose across the treatment

Yi Lao, Ph.D.[1], **Minsong Cao, Ph.D.**[1], **Yingli Yang, Ph.D.**[1], **Amar U. Kishan, M.D.**[1], **Wensha Yang, Ph.D.**[2], **Yalin Wang, Ph.D.**[3], **Ke Sheng, Ph.D.**[1]

[1]Department of Radiation Oncology, University of California - Los Angeles, USA

[2]Department of Radiation Oncology, University of Southern California, Los Angeles, USA

[3]School of Computing, Informatics, and Decision Systems Engineering, Arizona State University, Tempe, USA

Abstract

Purposes: To introduce a novel surface-based dose mapping method to improve quantitative bladder dosimetric assessment in prostate cancer (PC) radiotherapy.

Methods: Based on the planning and daily pre and post-fraction MRIs of 12 PC patients, bladder surface models (SM) were generated on manually delineated contours and regionally aligned via surface-based registration. Subsequently, bladder surface dose models (SDM) were created using face-wise dose sampling. To determine the bladder intrafractional and interfractional motion and dose variation, we performed a pose analysis between pre and post-fraction bladder SMs, as well as surface mapping for fractional SMs. Discrepancies between the received dose, accumulated from daily SDMs, and the planned dose were then assessed on the corresponding SDMs. Complementary to the surface dose mapping, dose-surface-histograms (DSHs) based comparisons were also performed.

Results: The intra-fraction pose analysis revealed a significant ($p<0.05$) bladder expansion, as well as an anterior/superior drift during the treatment. The intra-fraction motion substantially altered dose to mid-bladder body, but not the bladder surface areas distal to or contiguous with the target. A similar pattern of dose variations was also detected by inter-fraction comparisons. With surface registration to the common SM, the cumulative bladder dose significantly differs from the planned dose. The discrepancy is evident in the mid-posterior range that corresponds to a mid-to-high dose region. The received DSH significantly differs from the planned DSH after permutation correction ($p=0.0122$), while the overall surface-based comparison after multiple comparison correction is non-significant ($p=0.0800$).

Conclusions: We developed a novel surface-based intra- and inter-dose mapping framework applied to a unique daily MR dataset for image-guided radiotherapy. The framework identified

The telephone number, and the e-mail address of the corresponding author: 310-267-8979 (work), ksheng@mednet.ucla.edu, Address of the corresponding author: Department of Radiation Oncology, 200 Medical Plaza Driveway, #B265, Los Angeles, CA 90095.

Research data are stored in an institutional repository and will be shared upon request to the corresponding author.

The authors declare no conflicts of interest.

significant intra-fraction bladder positional changes, localized the intra- and inter-fraction variations, and quantified planned vs. received dose differences on the bladder surface. The result indicates the importance of adopting the motion-integrated bladder SDM for bladder dose management.

Keywords

Surface dose model; Surface-based registration; Bladder motions; Prostate Cancer

1 Introduction

Prostate cancer (PC) is the most prevalent cancers in men, affecting 11% of men in the US[1-2]. With the advances of therapeutic regimens, of which external beam radiotherapy (RT) is a mainstay treatment, the 5-year survival rate of prostate cancer patients has risen to over 98%[2]. The ten-year disease-free survival (DFS), as a more rigorous outcome metric for evaluating the efficacy of a local treatment modality for indolent cancer[3-4] is nearly 75%[5]. Therefore, treatment-related toxicities have risen to be a major concern for the high percentage of patients who survive cancer. Much of the focus in the past was on rectal toxicity, which has been markedly reduced with advanced therapy techniques, including intensity-modulated RT[6] and spacers[7]. However, genitourinary (GU) toxicity remains a major concern[8-16]. According to multiple clinical trials, the 5-year late grade ≥2 GU toxicity rates range from 12-15%[10-14], and the 10-year rate insidiously increases to 17-20% due to cumulative incidence[15-16]. The GU toxicity can be attributed to the high urethra and bladder doses that need to be addressed separately. The current study focuses on the bladder radiation dose-volume effect that has been reported for acute and late toxicity[17-18]. More recent studies have revealed anatomically localized dose-toxicity in the bladder, including dysuria, retention, hematuria, and incontinence[19-21]. On the other hand, these studies are based on the initial treatment plan that cannot accurately account for the actual cumulative dose received by the bladder due to its unique anatomical characteristics. First, the bladder is a hollow organ with urine filling. The commonly used dose-volume histogram (DVH) cannot correctly account for the dose to the bladder wall. Second, the bladder demonstrates substantial and rapid variations in its size, shape, and position. To better establish its radiobiology and protect the bladder, one must improve the accuracy of its cumulative dose characterization.

To address the first challenge that the bladder is a hollow organ, Carillo et al. demonstrated a software tool to tally the voxel doses on the bladder contour surface and generated dose surface histogram (DSH)[22]. Maggio et al. showed that the DSH was more consistent with the dose to the bladder wall than DVH[23]. It was concluded by Rosewell et al.[24] that “dose reconstruction with a hollow organ model is recommended if the goal is to associate that dose with toxicity”.

The second challenge is that the bladder is a highly variable organ influenced by urine filling, posture changes, and surrounding organ movement. Urine filling is partially controlled with procedures including pre-treatment water intake, but substantial residual bladder variation cannot be eliminated. For this reason, surface mapping of daily images

is necessary to accurately estimate the cumulative bladder surface dose. Deformable registration algorithms designed for the entire image assume 3D space continuity and are unsuited to register hollow organs that are not connected to its internal content[25-26]. Instead, a specialized method for surface registration was investigated[19-21]. For this purpose, Palorini et al. further applied the dose surface histogram tool to extract the bladder surface dose from daily MVCT images and reported dose variation on a projected 2D plane[27]. However, registration of the daily bladder surfaces was performed by unfolding the bladder to fit a rectangle, which created unrealistic bladder morphological changes and inaccuracies in cumulative dose estimation. To better preserve the anatomy in registration, Anderson et al. and Rosewall et al. modeled the bladder as empty surfaces and used surface-based biomechanical simulation for inter-scan dose accumulation[24,28]. The studies assume a constant Young's modulus 10 kPa and a Poisson's ratio 0.499 for all bladders. This is a significant simplification of the reported bladder wall Young's modulus ranging from 4 kPa to 260 kPa[29]. Also, the gravitational force of varying liquid filling was not modeled in the mechanical analysis. More accurate biomechanical registration would require individual patient mechanical properties that are difficult to obtain, preventing this method from being widely applicable for prostate radiotherapy. An image-based registration method for the unique bladder anatomy needs to be developed and tested on longitudinal 3D images.

To overcome these technical challenges in the bladder surface dose characterization, we introduce a novel surface-based bladder dose modeling framework. We then demonstrate its efficacy on fractionated MR-guided prostate radiotherapy images.

2 Materials and Methods

2.1 Patients and imaging data

With institutional review board approval, 12 post-prostatectomy patients receiving 5-fraction external beam RT were retrospectively solicited from our institutional database. Radiation treatment plans were designed to deliver 30–34 Gy in 5 fractions to the prostate bed such that 95% of the PTV received the prescription dose and all OAR dose constraints were met. If a gross tumor was visible on imaging, a gross tumor volume (GTV) was defined and expanded isotropically by 3–5 mm to form a PTVGross. This target could receive up to 40 Gy in five fractions with a simultaneous integrated boost. A treatment plan using 10–17 selected IMRT beams was generated using the ViewRay Treatment Planning System TPS (Version 5.4, ViewRay Inc. Cleveland, OH, USA), and the optimization was controlled by setting dose optimization parameters for the target and each OAR by the user. Dose calculation was performed with a grid resolution of 2 mm using a Monte Carlo-based algorithm that takes into account the MRI magnetic field effect on the dose distribution. Planning constraints for the OAR included bladder maximum dose (Dmax) <35.7 Gy, V32.5 Gy <35%; rectum Dmax <35.7 Gy, V27.5 Gy <45% and V32.5 Gy <30%, and rectal wall V24 Gy <50% that were derived from institutional constraints. For plans with the PTVGross, the bladder and rectum maximum dose were accepted if less than 39 Gy. The final prescription dose to the prostate bed was chosen in the range of 30–34 Gy to ensure all OAR dose constraints were met.

Each patient underwent one bSSFP MRI scan for RT planning, as well as 5 pre and 5 post-RT fraction balanced steady-state free precession (bSSFP) MRI scans for motion monitoring purposes. Three patients missed one of the post-RT scans due to personal issues, resulting in a total of 129 MRIs in the study. Patients were instructed to drink 16-24 oz water before each treatment fraction. All MRI scans were acquired with the onboard 0.35T MR as part of the ViewRay MRIdian LINAC (Mountain View, CA, USA). These onboard images have a field of view of 50 × 45 × 43 cm, an in-plane resolution of 1.5mm × 1.5mm, and slice thickness ranging from 1.5mm - 3mm. The total acquisition time ranges from 25 – 172s.

For each MRI scan, bladders were manually delineated by a physicist and verified by a radiation oncologist. For each patient, all treatment MRIs were first rigidly aligned to the planning MRI based on cross-correlation of the entire volume, and the resulted transformations were propagated onto the bladder contour. The planning bladders (P-bladder) and treatment bladders (T-bladders) were binarized and processed through the pipeline illustrated in Fig. 1.

2.2 Bladder surface dose modeling

2.2.1 Surface generation and registration—As shown in Fig. 1, a triangulated surface mesh was first generated on each binary bladder segmentation using the marching cube algorithm[30]. To obtain regional alignment on the bladder surface, and thus facilitate localized inter-bladder comparison and dose accumulation, we applied the constrained harmonic registration (CHR) on each bladder surface[31-33]. Specifically, due to the elongated shape of the bladder, the bladder surface mesh was preferably mapped to a topological cylinder with two open boundaries. With two topological constraints set at the anterior and posterior extreme positions, the 3D surface alignment was unfolded into a simple 2D registration problem, through which angle-preserving (conformal) grids were mapped onto bladder surfaces using holomorphic 1-form method[32-33]. Briefly, for a triangulated mesh surface S, a harmonic 1-form ω was derived iteratively by minimizing the harmonic energy:

$$E(\omega) = \sum_{[u,v] \in S} k_{u,v} \| \omega[u,v] \|^2 \quad (1)$$

where [u,v] represents an edge spanned by vertices u and v in S, $k_{u,v}$ is the edge weight defined as the summation of the cotangents of the corner angles in two adjacent faces sharing [u,v]. Equation (1) minimizes the difference between the tangent vector along ω and the principal direction (i.e., the principal boundary unfolding the surface), thus ensuring the conformality. Then, a holomorphic 1-form can be calculated by paring ω with its conjugate $*\omega$ following Hodge theorem, as: $\omega + \sqrt{-1}(*\omega)$[31]. A holomorphic 1-form induces a system of iso-curves called conformal net. Such induced conformal parameterization is always a diffeomorphism for a convex polygon, such as a cylinder. The mapping between two surfaces can be indirectly obtained via the mapping between the two corresponding parameterized spaces $\tau: \mathfrak{R}^2 \rightarrow \mathfrak{R}^2$, as[31-32]:

$$\tau \circ \tau_s(S_s) = \tau_t(S_t), \tau \circ \tau_s(\partial S_s) = \tau_t(\partial S_t), \Delta\tau = 0 \quad (2)$$

Where S_s, S_t, and $\tau_s: S_s \rightarrow \Re^2$, $\tau_t: S_t \rightarrow \Re^2$ represent the subject surface, the template surface, and the corresponding holomorphic 1-form induced conformal parameterizations, respectively. The one-to-one mapping between S_s and S_t, $\phi: S_s \rightarrow S_t$, can then be obtained via τ_s, τ_t, and τ, as τ_t^{-1}. As such, a surface model (SM) with aligned surface vertices and faces in original 3D space was generated for each bladder. Visualizations of the generated conformal grids and inter-fraction bladder surface alignment after surface-based registration can be found in Fig. 2(a).

To evaluate surface-based registration quality, we calculated displacements of landmarks after both rigid alignment and surface-based registration. Specifically, three landmarks, including the left and right ureters and urethral orifice openings, were manually placed on the planning and motion-monitoring MR. Due to the limited capability of clinical MR in visualizing urethral details, landmarks are placed only when scan-wise correspondences can be found with high confidence. In particular, rigid transformations obtained in section 2.1 were propagated onto landmarks defined on motion-monitoring scans, followed by which the Euclidean distance between transformed landmarks L_t, and the corresponding landmark in the planning MR, L_p were calculated as D_{rigid}. On each of the registered surface models from motion-monitoring scans, the surface vertex that is closest to L_t in the three-dimensional space are assigned as significant vertex and denoted S_t. Similarly, the corresponding significant vertex in the planning surface model can be found with respect to L_p, and denoted S_p. The Euclidean distance between S_t and S_p in the planning scan was calculated as D_{surf}. A comparison between D_{rigid} and D_{surf} is listed in Table 1. As shown in the table, for all three landmarks, surface-based CHR leads to consistently better alignments than rigid registration.

2.2.2 Surface dose sampling—To create a surface dose model (SDM), on each registered bladder surface model (SM), we interpolated local dose values from nearby relevant voxels (RV) in the small region-of-interest normal to the surface, emulating a sampling through the thickness of the bladder wall. RVs are defined as the voxels inside the prism shown in Fig. 2(c). Specifically, in Fig. 2(c), for a triangular face on the surface, t, with center c and normal $\vec{n}$, we constructed a small triangular prism, whose two triangular bases being two dilated faces, T mm apart from each other in the direction of $\vec{n}$. The vertices of the dilated face t', are R mm extended from the original center of c along the 3 medians of t. Since a 5mm artificial wall best surrogates the 'true' bladder wall in dose calculation, as shown in other studies[24], we chose T=5 mm in the study. Given the large voxel size, a dilation parameter of R=2.5 was select to avoid empty sampling.

The final surface dose value was interpolated through inverse distance weighting of RVs, as:

$$V(x) = \frac{\sum_{i=1}^{N} ID_i(x) V_i}{\sum_{i=1}^{N} ID_i(x)} \tag{3}$$

where

$$ID(x) = \left(\sum_{i=1}^{N} \frac{1}{d(x, V_i)^2} \right)^{\frac{1}{2}} \quad (4)$$

In the above equations, V_i represents the dose value for an RV i, $V(x)$ is the interpolated dose value for a surface face with center x. $ID_i(x)$ denotes the inverse distance weighting for the RV i to the surface face center x, in which $d(x, V_i)^2$ is the squared Euclidean distance between i and x.

2.3 Statistical analysis

To gain an insight into the bladder motion as the cause for dose deviations, we first probed into the anatomical changes induced by the change in filling. We then performed a surface dose comparison between two filling states and analysis of inter-fraction dose variation, with each fraction averaged from the low and high-filling models. Finally, we conducted an overall comparison between the planned dose and the received dose, summed from all the fractions.

2.3.1 Intra-fraction pose analysis between the low- and high-filling bladder SMs—

Based on MRI scans acquired pre and post-treatment, representing the bladders with an increasing filling level, we performed a global positional comparison of bladders between the low (pre-RT) and high-filling (post-RT) states. To perform the comparison in a common reference frame that excluded the irrelevant external positional information, i.e., variable location within the scanner, we performed inter-subject affine registration to transform all treatment MR images into a target MR scan, randomly selected from our dataset. The linear transformations were then propagated onto bladder surface models constructed in Sec. 2.2.1. The affine transformation coarsely aligns patients to the same image to prepare for the second step of fine surface registration. Therefore, the random selection of MR does not influence the final result.

The relative position of each bladder was obtained through the Procrustes fit, which globally aligns the surface model through the vertex-cloud without changing the shape[34-35]. To be specific, a full Procrustes alignment is defined as[36], $T(X) = (sRX, d)$, where s, R, and d represent the uniform scale factor, the 3×3 rotation matrix and the translation vector $(x, y, z)^T$, respectively. The alignment target is selected as the mean bladder shape averaged from all subjects, and the transformation is centered to the centroid of the mean shape.

The transformation parameters usually represented as a single matrix to facilitate batching multiplication, as in[37]:

$$T = \begin{pmatrix} sRX & d \\ 0^T & 1 \end{pmatrix} \quad (5)$$

The above matrix T form a Lie group, which resides in the Riemannian manifold where the integration of multiple similarity matrices is written as matrix multiplication instead of

value addition or subtraction, thus standard group comparison calculation does not apply. As a simplification, we used a log-Euclidean framework to map the matrices onto a tangent plane, where computations are conducted by matrix exponentials and logarithms; thus, the standard Euclidean space statistics can be directly applied[36,38-39]. The mean of all Procrustes transformations, a mean pose TM, is defined similarly to the Karcher mean in the Euclidean space[40], and can be calculated iteratively as[36,41]:

$$TM_{k+1} = TM_k exp\left(\frac{1}{n}\sum_{i=1}^{n} log\left(TM_k^{-1}T_i\right)\right) \quad (6)$$

where k is the estimation step, n represents the total number of subjects, and T_i denotes the Procrustes transformation for the i[th] subject. The mean pose TM was then subtracted from each T_i to generate a residual pose R_i, whose norm represents the Euclidean distance of each pose from the mean[36,41-42]. Specifically, as:

$$R_i = log(TM^{-1}T_i) \quad (7)$$

Subsequently, paired t-tests between the low- and high-filling groups were performed on the residual pose, in terms of 1 scale (s), 3 rotation (θ_x, θ_y, θ_z) and 3 translation (t_x, t_y, t_z) parameters.

2.3.2 Intra-fraction and inter-fraction dose variations—For each patient, 10 regionally aligned surface dose models (SDM) were generated based on the daily acquired pre and post-RT bladder contours, according to Sec. 2.2.1 and 2.2.2.

Intra-fraction comparisons between low-filling and high-filling SDMs, generated based on pre and post-RT scans, were conducted in terms of localized surface doses and the resultant dose surface histograms (DSH). Firstly, paired t-tests were performed at each surface triangular-face between all the low-filling and the corresponding high-filling SDMs from all patients. Given the limited sample size and a large number of face-wise comparisons, 10000 nonparametric permutations were performed in two aspects: 1) on each face-wise t-test, to avoid a normal distribution assumption; 2) on the extent of overall significance containing all face-wise t-tests, to correct for multiple comparisons[43-45]. The permutation was followed by bin-wise paired group comparisons between the low-filling and high-filling DSHs. Similarly, 10000 nonparametric permutations were conducted at each bin of DSHs, as well as globally on all bins.

Apart from the intra-fraction analysis, inter-fraction dose variations were also analyzed in terms of localized surface doses on fractional SDMs, each generated by an average of the corresponding pre and post-RT SDMs, and the resultant DSHs. Specifically, on each local triangular face of the SDM, fractional mean (average of all fractions from all patients), population S.D. (standard deviation of individual inter-fraction standard deviations), and relative population S.D. (population S.D. divided by the mean) were calculated. Besides, on DSHs generated for all fractional SDMs, bin-wise fraction means and population S.D. were estimated.

2.3.3 Planned and accumulated dose comparisons—

For each patient, a planned SDM was generated based on the bladder segmentation from the planning MRI scan as in Sec. 2.2.1 and 2.2.2. The received SDM of each patient was calculated by a face-wise accumulation of the corresponding fractional SDM generated above. Similar to the comparison between low- and high-filling status, face-wise paired t-tests were conducted between the planned and the received SDMs from all patients, followed by bin-wise comparisons of DSHs between these two groups. Distributional bias and multiple comparison errors were corrected in both comparisons, each with 10000 nonparametric permutations, as done in the previous section[43-45].

3 Results

3.1 Intra-fraction low- and high-filling pose changes

Results of the pose analysis between the low- (pre-RT) and high-filling (post-RT) SMs are shown in Table 2. The low- and high-filling SMs presented significant differences in the scale (s), rotation (θ_x), and translation (t_y, t_z) scalars. The results can be better visualized in Fig. 3, where the mean shapes of the low- and high-filling SMs are superimposed. The mean shape of high-filling SMs was significantly larger than that of the low-filling ones. The volume change is accompanied by an evident shift in both the anterior-posterior (y) and the inferior-superior (z) directions. Besides, the mean shape of the high-filling group positioned slightly rightward to that of the low-filling group, consistent with the significant p-value in θ_x. The shifts in other rotational and translation axes were insignificant.

3.2 Inter-fraction and intra-fraction analyses

As shown in Fig. 4, the results of the inter-fraction analysis were projected onto the mean shape averaged from all subjects. In particular, the mean fraction dose (Fig. 4(a)), averaged from all patients, was the highest in the posterior bottom of the bladder due to its abutment with the target. The dose gradually decreases towards the anterior upper end. The absolute population standard deviation (S.D.) (Fig. 4(b)) tended to be lower in two extreme ends and higher in the middle body of the bladder. When normalized by the local mean dose, the relative population S.D. (Fig. 4(c)) was the highest in the upper anterior end and gradually decreased toward the posterior bottom, which was opposite to the trend of the mean dose. The non-uniform distributed inter-fraction dose variations were further confirmed by the DSHs shown in Fig. 6(a), where DSH curves fluctuated greatly in low-to-medium dose regions and converged toward the high dose regions.

Discrepancies between intra-fraction low-filling (pre-RT) and high-filling (post-RT) SDMs were illustrated in (Fig. 4(d)), where surface doses in the low-filling group were, on average, up to 1 Gy higher than those from the high-filling group. Group comparison between these two groups (Fig. 4(e)) showed widespread significances encompassing the body of the bladder, excluding the posterior base and the superior center – the two regions falling into the highest and the lowest dose regions, respectively. After multiple comparison corrections, the overall p-value of the low- and high-filling SDM comparisons was < 0.0001. The widespread group differences were also reflected in their DSHs (Fig. 5(a-c)), where the low-filling group exhibited significantly higher concentration in a wide span of the middle

dose range. The bin-wise comparison resulted in an overall significance of $p < 0.0001$, after multiple comparison corrections.

3.3 The planned and received dose comparisons

Discrepancies between the planned and the received dose surface doses can be found in Fig. 6. In particular, all three example patients in Fig. 6(a) show varied extent of 'dose-averaging' effect in the mid body of the bladder, where the high doses are spreaded into a larger bladder surface. Averaged from all patients, the mean of the daily accumulated surface doses was evidently lower (up to 5 Gy) than that of the planned doses in the inferior side of the bladder body and was slightly higher (up to 2 Gy) in the superior center (Fig. 6(b)). As shown in Fig. 6(c), these discrepancies remained significant after face-wise nonparametric permutation correction, while the majority of the posterior and anterior ends present little or no differences. The overall surface dose comparison between the planned and the received SDMs, after multiple comparison corrections, resulting in a low, albeit non-significant, a global p-value of 0.0800. The planned vs. received comparisons can also be visualized in DSHs (Fig. 5(d)), where the daily accumulated DSHs were on average higher than the planned ones in the low dose range (0-10 Gy) and lower than the planned ones in the medium to high dose range (10-35 Gy). The significant group differences, after permutation correction, concentrated in the moderate to high dose range (25-32 Gy) that corresponding to the middle-to-posterior body of the bladder, with a few spotted in two extreme ends (Fig. 5(e)). After multiple comparison corrections, the overall bin-wise DSH comparisons resulted in a significant p-value of 0.0112.

3.4 Discussion

In the current study, we implemented a pipeline of conformal surface mapping for bladder dose modeling and localized dosimetric analysis. Through surface-based constrained harmonic registration, the local geometric alignment algorithm allowed us to establish inter-scan correspondences of each of the surface vertices[31-32,48-49] and facilitate subsequent face-wise accumulations and comparisons. Utilizing the MRI scans acquired before and after each fraction, as two representative filling states, we were able to estimate the cumulative bladder dose accounting for both intra- and inter-fraction bladder variations.

The current study is also the first to characterize the bladder motion patterns using statistical pose analysis for dosimetric correlation. The anterior/inferior motion of the bladder is restricted by the rigid pubis. Its superior end motion is only limited by the flexible peritoneum and is less confined. Subsequently, as shown by the pose comparisons between low- and high-filling surface models, the bladder deformation had a significant anterior/superior directional preference with increased filling. This is consistent with the findings in fractional surface dose comparisons, where the regions with the most displacement (shown in Fig.3), the apex area, were the regions with the highest normalized inter-fractional S.D.(Fig. 4(c)). However, since these regions are distal from the RT target, there is a smaller effect on the final accumulated dose maps. The intra-fraction dose comparisons demonstrated large dose variations in the mid-bladder surface that presented a mid-level displacement in motion and exposed to mid-high radiation dose. The large mid-bladder surface dose variations were also shown in the inter-fraction registration analysis. The

results are consistent with the findings from other DVH or 2D grid-based inter-fraction analyses[27,50]. It is worth noting that not all patients follow the populational trends. Fig. 6(a) exemplified individual differences: the planned high dose volumes (regions colored in red) for patients 1 and 3 expanded and contracted, respectively, while patient 2 showed minimal changes. The result highlights the importance of performing personalized image-guided surface registration.

The improved registration accuracy should help establish more reliable regional dose-symptoms relationships for guiding future radiotherapy planning practice. For example, the mid-bladder surface dose was associated with an increased incidence of toxicity in one study[19] but not the other[20], both based their analysis on the static planning images. The discrepancy in observation could be due to the inter and intra-fractional bladder motion and resultant deviation of the received mid-bladder wall dose from the planned dose, which is better captured with our CHR mapping of daily MR images. The accurate cumulative dose information can be used to design sub-surface structures in online adaptive radiotherapy for better control of the total dose to the bladder wall and avoid undesired cumulative hot spots that may cause acute and long-term toxicities.

Several model parameters can influence our results. **(i), the number of surface triangles n**. In the study by Xiong et al., an n=8192 triangular mesh can better represent geometrical features of a bladder and yield higher registration accuracy compared with 2000 or fewer triangles[46]. More triangles, in theory, improve the accuracy of surface representation but require longer registration and sampling time. Here in this study, we used 29502 triangles, which were shown adequate to represent similarly shaped structures and at the same time computationally affordable[39,48-49]. Given that our surface triangles/faces are substantially more than the dose voxels, further increasing mesh triangles would have a diminishing return. **(ii), the dilation parameter R** in the sampling triangular prism. Using a too large R will lead to an overly smoothed dose distribution, thus reducing the subsequent detection sensitivity to smaller dose variations. On the contrary, give the in-plane dimension of 1.5 mm × 1.5 mm and slice thickness up to 3 mm, using an R smaller than 2.5 will lead to empty sampling in some curved surface locations. **(iii), the surrogate thickness T** for including the ‘relevant voxels’. The mean bladder wall thickness is over 3 mm for adults, and the upper limit was reported to be 5mm for children[51-52]. The thickness was found to increase with age, while the exact number for the same person may change according to different distention levels[51-52]. A previous study modeling bladder wall dose showed that 5mm artificial wall best surrogates the 'true' bladder wall in dose calculation[24]. Thus, T= 5mm was chosen as a limit to include ‘relevant voxels’. The inverse distance-based sampling scheme is insensitive to voxels farther from the bladder surface.

The present study is not without its weaknesses. **First,** the study dataset is limited by the number of patients with complete planning, pre, and post-treatment MRI images. Although the permutation-based correction applied on each paired t-test partially corrects for a normal distribution assumption, the synthetic' normal' distribution from permuting the existed samples cannot fully represent a 'true' large cohort. Therefore, some of the findings, for instance, the unexplained θ_x changes in the pose analysis, should be taken with caution, pending further validations from a future larger dataset. **Second,** the harmonic registration

method strongly depends on the boundary conditions or the selection of constraints. Due to the lack of stable and MRI visible geometric anchors on the bladder surface, we set the constraints at the anterior and posterior extreme positions, which are shown to be the regions with the most and least movements in motion, thus yielding stable correspondences across subjects[27,53]. If ureter and urethra orifices are used to anchor the registration, they cannot be reused for registration validation to avoid confirmation bias. Moreover, as the mapping target, the topological cylinder is a good but not perfect representation of the bladder. Previous experience on elongated structures with similar shapes (i.e., thalamus and putamen in the brain) showed that mapping to a cylinder space, other than a canonical sphere space, reduces distortions and, thus, is more anatomical correlated alignment[31-32,45]. Although all studied bladders yield qualitatively and quantitatively consistent registration, a structure-specific surface template generated on higher resolution images of a larger sample size may further improve the surface registration results. **Third,** we used an artificial wall structure with uniform thickness for surface dose sampling. The fixed-thickness or thick-less surfaces have been validated as good surrogates for bladder walls in histogram-based comparisons[23, 50]. However, the bladder wall thickness and expansion/contraction due to filling changes can be heterogeneous, resulting in a different estimated bladder dose than that of the current uniform thickness model. Although the difference is likely small, future image studies that are capable of quantifying the bladder wall thickness and changes may provide a more accurate assessment for RT dose management. **Finally,** validating bladder surface registration is intrinsically difficult due to the scarcity of landmarks on bladders. Xiong et al. used the left and right bladder-ureter and bladder-urethra junctions as the only unambiguous landmarks[46]. We used the same three anatomical landmarks. Our results are consistently better than the common clinical practice using rigid registration and comparable/slightly superior to Xiong et al. The residual landmark misalignment is collectively contributed by registration error and landmark placement uncertainty. Unlike Xiong et al.[46], which used high-resolution diagnostic CT for registration and validation, our study was performed on images from 0.35T MRgRT, which provides daily 3D anatomical images with superior soft-tissue contrast but lower resolution for landmark annotation. The localization confidence is further affected by noise in the low field MR. The residual misalignment could affect the quantitative assessment of bladder surface dose in the high dose gradient region. Besides higher quality MR images acquired with improved sequence and reconstruction, a deformable bladder phantom study with dense landmarks should be valuable for comprehensive validation.

4 Conclusion

In this study, we introduced a novel surface-based bladder dose modeling for PC patients treated with fractioned SBRT. Based on daily MRI scans obtained pre and post-fraction, for the first time, we identified significant intra-fraction positional changes using bladder surface models and quantified the intra- and inter-fraction dose variations on the bladder surface. The motion-integrated bladder surface doses significantly deviated from the planned dose in the mid-posterior section of the inferior bladder wall. The result indicates the need to include both intra- and inter-fractional bladder motion management in adaptive prostate RT.

Acknowledgment

The study was supported in part by the AAPM Seed Fund and NIH R01CA188300.

This research did not receive any specific grant from funding agencies in the public, commercial, or not-for-profit sectors.

7. References

[1]. Fitzmaurice C, Allen C, Barber RM, Barregard L, Bhutta ZA, Brenner H, Dicker DJ, Chimed-Orchir O, Dandona R, Dandona L, Fleming T Global, regional, and national cancer incidence, mortality, years of life lost, years lived with disability, and disability-adjusted life-years for 32 cancer groups, 1990 to 2015: a systematic analysis for the global burden of disease study. JAMA Oncol. 2017; 3(4): 524–548. [PubMed: 27918777]

[2]. Siegel RL, Miller KD, Jemal A Cancer statistics, 2018. CA Cancer J Clin. 2019; 68:7–30.

[3]. Grimm P, Billiet I, Bostwick D, Dicker AP, Frank S, Immerzeel J, Keyes M, Kupelian P, Lee WR, Machtens S and Mayadev J, Comparative analysis of prostate-specific antigen free survival outcomes for patients with low, intermediate and high risk prostate cancer treatment by radical therapy. Results from the Prostate Cancer Results Study Group. BJU Int, 2012; 109:22–29.

[4]. Sweeney C, Xie W, Regan MM, Nakabayashi M, Buyse ME, Clarke NW, Collette L, Dignam JJ, Fizazi K, Habibian M and Halabi S, Disease-free survival (DFS) as a surrogate for overall survival (OS) in localized prostate cancer (CaP). J. Clin. Oncol 2016; 34(15):suppl 5023.

[5]. Critz FA, Benton JB, Shrake P and Merlin ML, 2013. 25-Year disease-free survival rate after irradiation for prostate cancer calculated with the prostate specific antigen definition of recurrence used for radical prostatectomy. J Urol. 2013; 189(3):878–883. [PubMed: 23103235]

[6]. Anderson NS, James BY, Peschel RE and Decker RH, A significant decrease in rectal volume and diameter during prostate IMRT. Radiother Oncol. 2011; 98(2):187–191. [PubMed: 21269715]

[7]. Mariados N, Sylvester J, Shah D, Karsh L, Hudes R, Beyer D, Kurtzman S, Bogart J, Hsi RA, Kos M and Ellis R, Hydrogel spacer prospective multicenter randomized controlled pivotal trial: dosimetric and clinical effects of perirectal spacer application in men undergoing prostate image guided intensity modulated radiation therapy. Int. J. Radiat. Oncol. Biol. Phys 2015; 92(5):971–977. [PubMed: 26054865]

[8]. Matta R, Chapple CR, Fisch M, Heidenreich A, Herschorn S, Kodama RT, Koontz BF, Murphy DG, Nguyen PL, Nam RK. Pelvic Complications After Prostate Cancer Radiation Therapy and Their Management: An International Collaborative Narrative Review. Eur Urol. 2019; 75(3):464–76. [PubMed: 30573316]

[9]. Brand DH, Tree AC, Ostler P, van der Voet H, Loblaw A, Chu W, Ford D, Tolan S, Jain S, Martin A, Staffurth J. Intensity-modulated fractionated radiotherapy versus stereotactic body radiotherapy for prostate cancer (PACE-B): acute toxicity findings from an international, randomised, open-label, phase 3, non-inferiority trial. Lancet Oncol. 2019; 20(11):1531–1543. [PubMed: 31540791]

[10]. Michalski JM, Moughan J, Purdy J, Bosch W, Bruner DW, Bahary JP, Lau H, Duclos M, Parliament M, Morton G, Hamstra D. Effect of Standard vs Dose-Escalated Radiation Therapy for Patients With Intermediate-Risk Prostate Cancer: The NRG Oncology RTOG 0126 Randomized Clinical Trial. JAMA Oncol. 2018; 4(6):e180039. [PubMed: 29543933]

[11]. Meier RM, Bloch DA, Cotrutz C, Beckman AC, Henning GT, Woodhouse SA, Williamson SK, Mohideen N, Dombrowski JJ, Hong RL, Brachman DG. Multicenter trial of stereotactic body radiation therapy for low-and intermediate-risk prostate cancer: survival and toxicity endpoints. Int. J. Radiat. Oncol. Biol. Phys 2018; 102(2):296–303. [PubMed: 30191864]

[12]. Spratt DE, Pei X, Yamada J, Kollmeier MA, Cox B, Zelefsky MJ. Long-term survival and toxicity in patients treated with high-dose intensity modulated radiation therapy for localized prostate cancer. Int. J. Radiat. Oncol. Biol. Phys 2013; 85(3):686–692. [PubMed: 22795805]

[13]. Ohri N, Dicker AP, Showalter TN. Late toxicity rates following definitive radiotherapy for prostate cancer. Can Urol Assoc J. 2012;19(4):6373–80.

[14]. Byrne K, Hruby G, Kneebone A, Whalley D, Guo L, McCloud P, Eade T. Late genitourinary toxicity outcomes in 300 prostate cancer patients treated with dose-escalated image-guided intensity-modulated radiotherapy. Clin. Oncol 2017; 29(9):617–625.

[15]. Widmark A, Gunnlaugsson A, Beckman L, Thellenberg-Karlsson C, Hoyer M, Lagerlund M, Kindblom J, Ginman C, Johansson B, Björnlinger K, Seke M. Ultra-hypofractionated versus conventionally fractionated radiotherapy for prostate cancer: 5-year outcomes of the HYPO-RT-PC randomised, non-inferiority, phase 3 trial. Lancet. 2019; 394(10196):385–395. [PubMed: 31227373]

[16]. Michalski JM, Moughan J, Purdy J, Bosch W, Bruner DW, Bahary JP, Lau H, Duclos M, Parliament M, Morton G, Hamstra D. Effect of standard vs dose-escalated radiation therapy for patients with intermediate-risk prostate cancer: the NRG oncology RTOG 0126 randomized clinical trial. JAMA Oncol. 2018; 4(6):e180039. [PubMed: 29543933]

[17]. Cheung MR, Tucker SL, Dong L, De Crevoisier R, Lee AK, Frank S, Kudchadker RJ, Thames H, Mohan R and Kuban D, Investigation of bladder dose and volume factors influencing late urinary toxicity after external beam radiotherapy for prostate cancer. Int. J. Radiat. Oncol. Biol. Phys 2007; 67(4):1059–1065. [PubMed: 17241755]

[18]. Viswanathan AN, Yorke ED, Marks LB, Eifel PJ and Shipley WU, Radiation dose–volume effects of the urinary bladder. Int. J. Radiat. Oncol. Biol. Phys 2010; 76(3):S116–S122. [PubMed: 20171505]

[19]. Yahya N, Ebert MA, House MJ, Kennedy A, Matthews J, Joseph DJ and Denham JW, Modeling urinary dysfunction after external beam radiation therapy of the prostate using bladder dose-surface maps: evidence of spatially variable response of the bladder surface. Int. J. Radiat. Oncol. Biol. Phys 2017; 97(2):420–426. [PubMed: 28068247]

[20]. Mylona E, Acosta O, Lizee T, Lafond C, Crehange G, Magné N, Chiavassa S, Supiot S, Arango JDO, Campillo-Gimenez B and Castelli J, Voxel-based analysis for identification of urethrovesical subregions predicting urinary toxicity after prostate cancer radiation therapy. Int. J. Radiat. Oncol. Biol. Phys 2019; 104(2):343–354. [PubMed: 30716523]

[21]. Marcello M, Denham JW, Kennedy A, Haworth A, Steigler A, Greer PB, Holloway LC, Dowling JA, Jameson MG, Roach D and Joseph DJ, Increased Dose to Organs in Urinary Tract Associates With Measures of Genitourinary Toxicity in Pooled Voxel-Based Analysis of 3 Randomized Phase III Trials. Front. Oncol 2020; 10:1174. [PubMed: 32793485]

[22]. Carillo V, Cozzarini C, Chietera A, Perna L, Gianolini S, Maggio A, Botti A, Rancati T, Valdagni R, Fiorino C. Correlation between surrogates of bladder dosimetry and dose–volume histograms of the bladder wall defined on MRI in prostate cancer radiotherapy. Radiother Oncol. 2012; 105(2):180–183. [PubMed: 23182056]

[23]. Maggio A, Carillo V, Cozzarini C, Perna L, Rancati T, Valdagni R, Gabriele P, Fiorino C. Impact of the radiotherapy technique on the correlation between dose–volume histograms of the bladder wall defined on MRI imaging and dose–volume/surface histograms in prostate cancer patients. Phys Med Biol. 2013; 58(7):N115. [PubMed: 23475338]

[24]. Rosewall T, Wheat J, Currie G, Kong V, Bayley AJ, Moseley J, Chung P, Catton C, Craig T, Planned versus 'delivered' bladder dose reconstructed using solid and hollow organ models during prostate cancer IMRT. Radiother Oncol. 2016; 119 (3):417–422. [PubMed: 27072936]

[25]. Lim K, Stewart J, Kelly V, Xie J, Brock KK, Moseley J, Cho YB, Fyles A, Lundin A, Rehbinder H and Löf J, Dosimetrically triggered adaptive intensity modulated radiation therapy for cervical cancer. Int. J. Radiat. Oncol. Biol. Phys 2014; 90(1):147–154. [PubMed: 25015200]

[26]. Nassef M, Simon A, Cazoulat G, Duménil A, Blay C, Lafond C, Acosta O, Balosso J, Haigron P and De Crevoisier R, Quantification of dose uncertainties in cumulated dose estimation compared to planned dose in prostate IMRT. Radiother Oncol. 2016; 119(1):129–136. [PubMed: 26993416]

[27]. Palorini F, Botti A, Carillo V, Gianolini S, Improta I, Iotti C, Rancati T, Cozzarini C, Fiorino C. Bladder dose–surface maps and urinary toxicity: Robustness with respect to motion in assessing local dose effects. Phys Med. 2016; 32(3):506–511. [PubMed: 27053449]

[28]. Andersen ES, Muren LP, Sørensen TS, Noe KØ, Thor M, Petersen JB, Høyer M, Bentzen L and Tanderup K, Bladder dose accumulation based on a biomechanical deformable image registration algorithm in volumetric modulated arc therapy for prostate cancer. Phys. Med. Biol 2012; 57(21):7089. [PubMed: 23051686]

[29]. Nenadic IZ, Qiang B, Urban MW, de Araujo Vasconcelo LH, Nabavizadeh A, Alizad A, Greenleaf JF, Fatemi M. Ultrasound bladder vibrometry method for measuring viscoelasticity of the bladder wall. Phys Med Biol. 2013; 58(8):2675–95. [PubMed: 23552842]

[30]. Lorensen WE, Cline HE. Marching cubes: A high resolution 3D surface construction algorithm. ACM siggraph computer graphics. 1987; 21(4):163–169.

[31]. Wang Y, Song Y, Rajagopalan P, An T, Liu K, Chou YY, Gutman B, Toga AW, Thompson PM, Alzheimer's Disease Neuroimaging Initiative. Surface-based TBM boosts power to detect disease effects on the brain: an N= 804 ADNI study. Neuroimage. 2011; 56(4):1993–2010. [PubMed: 21440071]

[32]. Wang Y, Lui LM, Gu X, Hayashi KM, Chan TF, Toga AW, Thompson PM and Yau ST, Brain surface conformal parameterization using Riemann surface structure. IEEE Trans Med Imaging. 2007; 26(6):853–865. [PubMed: 17679336]

[33]. Gu X and Yau ST, Computing conformal structure of surfaces. arXiv preprint. 2002; cs/0212043.

[34]. Dryden IL. and Mardia KV. Statistical shape analysis. John Wiley and Sons, Chichester.1998.

[35]. Ross A Procrustes analysis. Course report, Department of Computer Science and Engineering, University of South Carolina. 2004.

[36]. Bossa M, Zacur E, Olmos S. Statistical analysis of relative pose information of subcortical nuclei: application on ADNI data. Neuroimage. 2011; 55(3):999–1008. [PubMed: 21216295]

[37]. Bossa MN, Olmos S. Statistical model of similarity transformations: Building a multi-object pose. IEEE CVPRW. 2006; pp. 59.

[38]. Arsigny V, Commowick O, Pennec X, Ayache N. A log-euclidean framework for statistics on diffeomorphisms. MICCAI. 2006; pp. 924–931.

[39]. Lao Y, Shi J, Wang Y, Ceschin R, Hwang D, Nelson MD, Panigrahy A, Leporé N. Statistical analysis of relative pose of the thalamus in preterm neonates. MICCAI workshop on Clinical Image-based Procedures, 2013; pp. 1–9.

[40]. Karcher H Riemannian center of mass and mollifier smoothing. Commun Pure Appl Math. 1977; 30(5):509–541.

[41]. Pennec X, Fillard P, Ayache N. A Riemannian framework for tensor computing. Int J Comput Vis. 2006; 66(1):41–66.

[42]. Lao Y, Gajawelli N, Haas L, Wilkins B, Hwang D, Tsao S, Wang Y, Law M, Leporé N. 3D pre-versus post-season comparisons of surface and relative pose of the corpus callosum in contact sport athletes. SPIE Medical Imaging 2014: Image Processing. 2014; 9034:90344E–1.

[43]. Nichols TE, Holmes AP. Nonparametric permutation tests for functional neuroimaging: a primer with examples. Hum Brain Mapp. 2002; 15(1):1–25. [PubMed: 11747097]

[44]. Lepore N, Brun C, Chou YY, Chiang MC, Dutton RA, Hayashi KM, Luders E, Lopez OL, Aizenstein HJ, Toga AW, Becker JT. Generalized tensor-based morphometry of HIV/AIDS using multivariate statistics on deformation tensors. IEEE Trans Med Imaging. 2007; 27(1):129–141.

[45]. Lao Y, Wang Y, Shi J, Ceschin R, Nelson MD, Panigrahy A, Leporé N. Thalamic alterations in preterm neonates and their relation to ventral striatum disturbances revealed by a combined shape and pose analysis. Brain Struct Funct. 2016; 221(1):487–506. [PubMed: 25366970]

[46]. Xiong L, Viswanathan A, Stewart AJ, Haker S, Tempany CM, Chin LM, Cormack RA. Deformable structure registration of bladder through surface mapping. Med Phys. 2006; 33(6Part1):1848–1856. [PubMed: 16872092]

[47]. Chai X, van Herk M, van de Kamer JB, Hulshof MC, Remeijer P, Lotz HT and Bel A, Finite element based bladder modeling for image-guided radiotherapy of bladder cancer. Med Phys. 2011; 38(1):142–150. [PubMed: 21361183]

[48]. Lao Y, Nguyen B, Tsao S, Gajawelli N, Law M, Chui H, Weiner M, Wang Y, Leporé N. A T1 and DTI fused 3D corpus callosum analysis in MCI subjects with high and low cardiovascular risk profile. Neuroimage Clin. 2017; 14:298–307. [PubMed: 28210541]

[49]. Lao Y, David J, Mirhadi A, Lepore N, Sandler H, Wang Y, Tuli R, Yang W. Discriminating lung adenocarcinoma from lung squamous cell carcinoma using respiration-induced tumor shape changes. Phys Med Biol. 2018; 63(21):215027. [PubMed: 30403196]

[50]. Fuchs F, Habl G, Devečka M, Kampfer S, Combs SE, Kessel KA. Interfraction variation and dosimetric changes during image-guided radiation therapy in prostate cancer patients. Radiat Oncol J. 2019; 37(2):127. [PubMed: 31137087]

[51]. Hakenberg OW, Linne C, Manseck A and Wirth MP, Bladder wall thickness in normal adults and men with mild lower urinary tract symptoms and benign prostatic enlargement. Neurourol. Urodyn. 2000; 19(5):585–593. [PubMed: 11002301]

[52]. Jequier S and Rousseau O, Sonographic measurements of the normal bladder wall in children. AJR Am J Roentgenol. 1987; 149(3):563–566. [PubMed: 3303881]

[53]. Hoogeman MS, Peeters ST, de Bois J, Lebesque JV. Absolute and relative dose–surface and dose–volume histograms of the bladder: which one is the most representative for the actual treatment?. Phys Med Biol. 2005; 50(15):3589. [PubMed: 16030384]

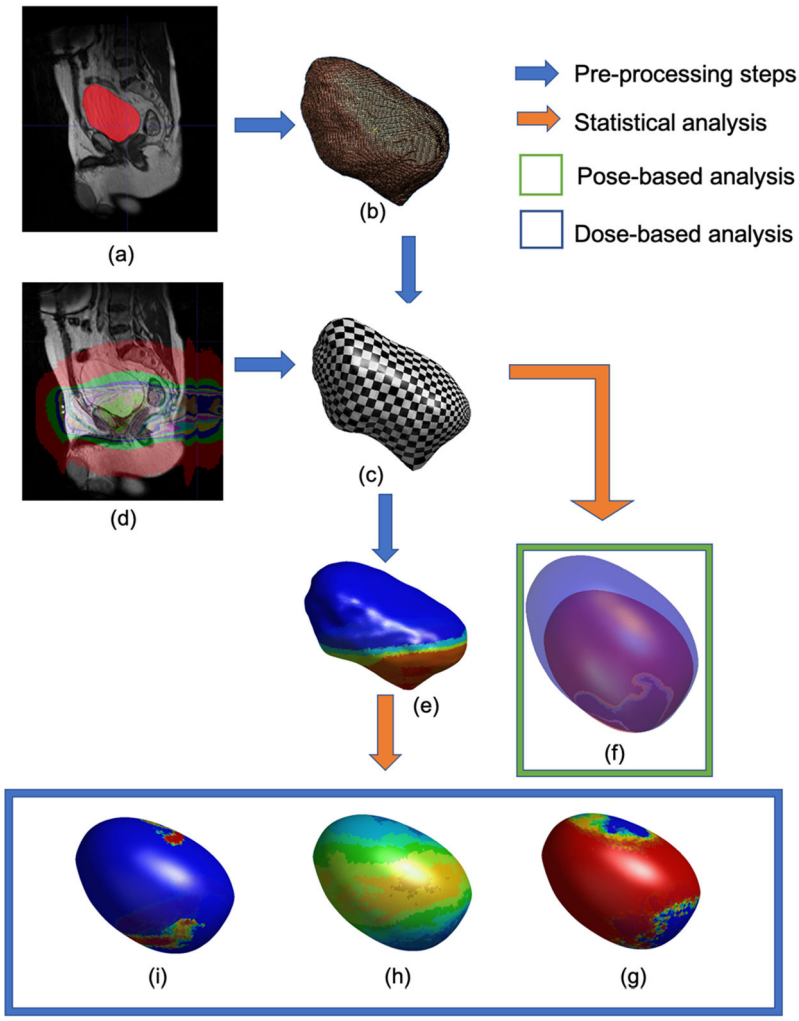

Figure 1:

Illustration of the proposed pipeline for surface-based modeling and statistical analysis. Based on the binary segmentation of the bladder (a), a surface mesh (b) was constructed. Through surface-based registration, point-wise correspondences were obtained on the bladder surface model (SM) (c), where the planning doses (d) were sampled and generated the surface dose model (SDM) (e). On SMs, an intra-fraction pose comparison was conducted (f). On SDMs, intra-fraction (g), inter-fraction (h), and the planned vs. received (i) dose comparisons were performed.

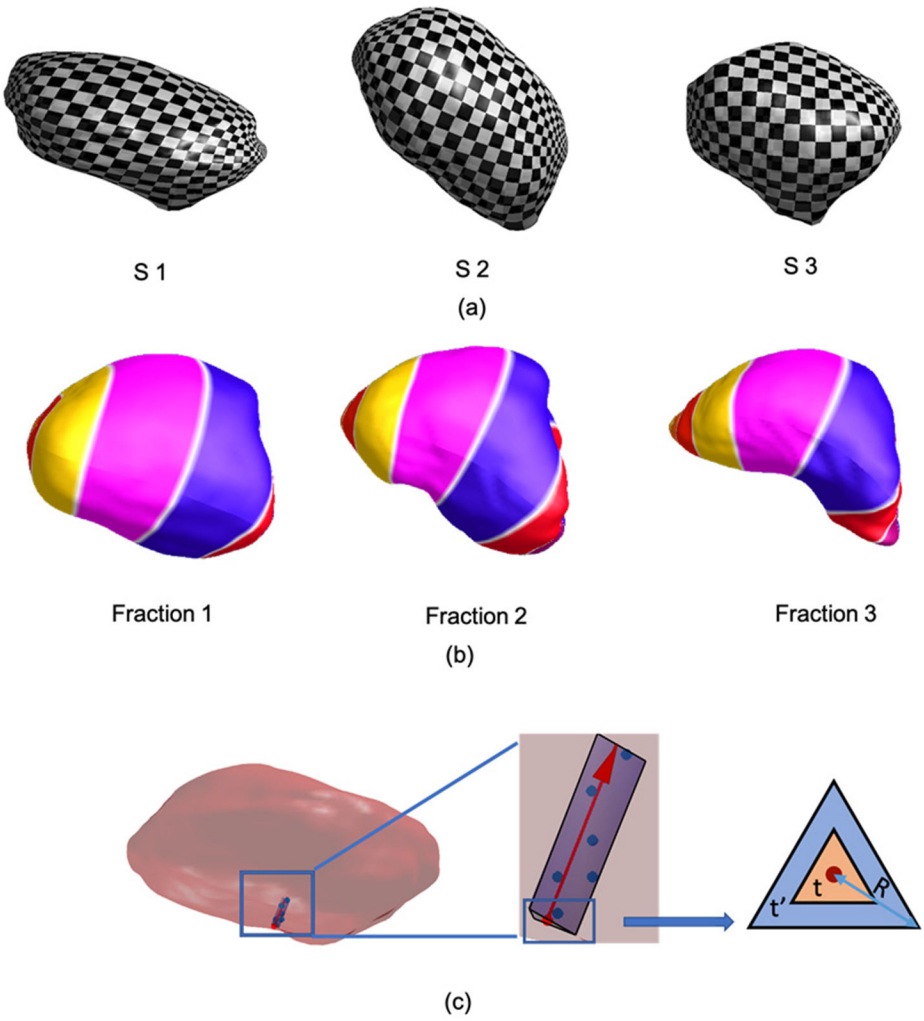

Figure 2:

Visualization of Registration and dose sampling schemes. (a) the holomorphic 1- form induced conformal grids for 3 patients. The conformality of the parameterization can be visualized by the checkerboard texture maps: orthogonal grids running in the cylindrical surface are mapped as right-angled checkboard lattices on the bladder. (b) inter-bladder alignment after surface-based registration for a sample patient in 3 different filling states. Corresponding regions in (b), coded by the same colors, are properly aligned with respect to the underlying anatomy. (c) the surface dose sampling scheme for one triangular face. In the zoomed view on the middle, the red dot and arrow represent the centroid c and the normal $\vec{n}$ of the face to be interpolated, respectively. The purple shaded area denotes the triangular prism, and dark blue dots are the sampled RVs. The right figure shows a bottom view of the prism.

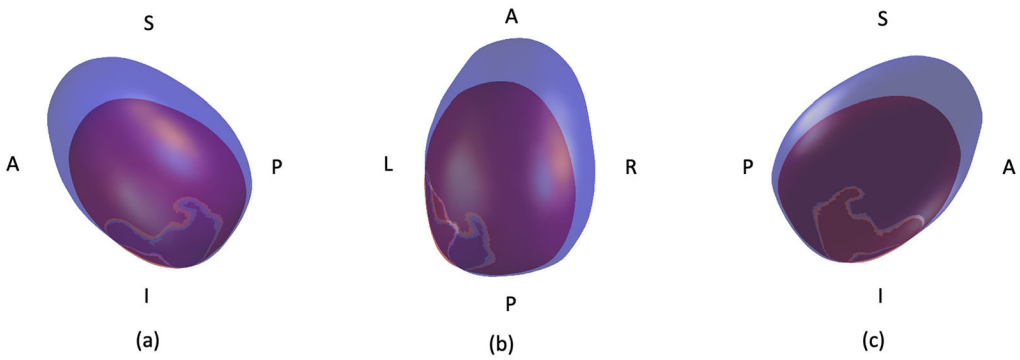

Figure 3:

3D visualization of the mean shapes averaged from the low-filling (red) and the high-filling (blue) SMs viewed from the left (a), top(b), and right (c) directions. The two groups present an evident inferior-superior shift and size changes, while pose changes in terms of rotation and translation in the other two directions are less visible. A-anterior, P-posterior, S-superior, I-inferior.

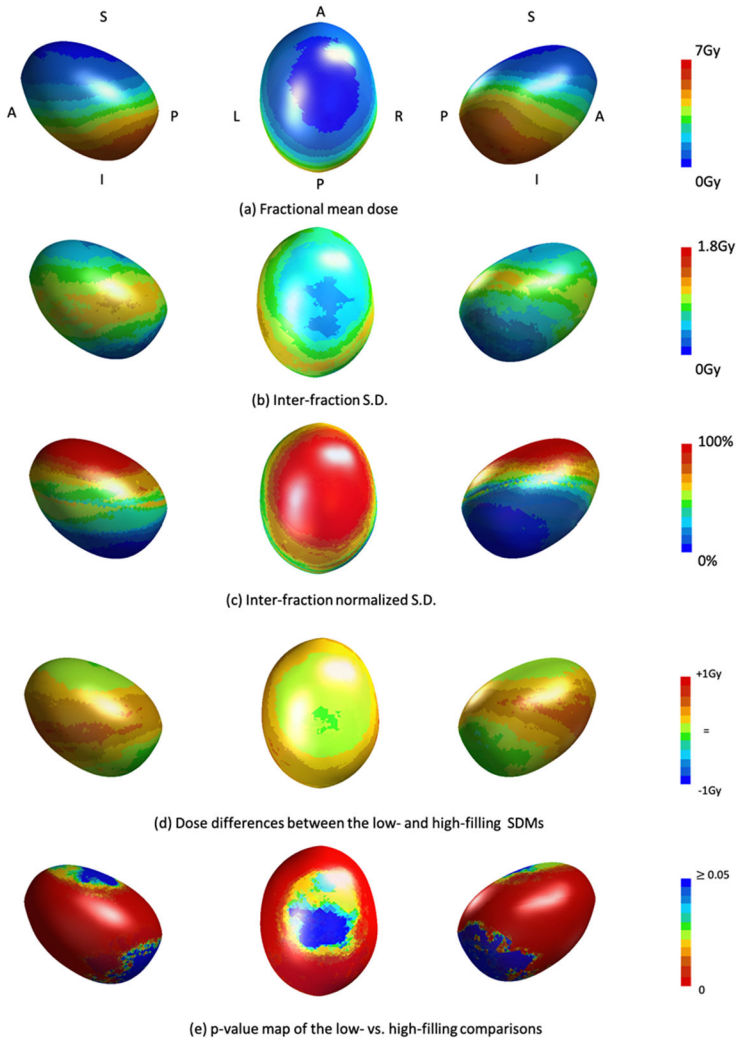

Figure 4:

Illustration of surface distributions of mean fraction dose (a), inter-fraction S.D. of dose (b), normalized inter-fraction S.D. of dose (c), averaged dose difference between low-filling (pre-RT based) model and high-filling (post-RT based) model (d), and p-values of low vs. high filling dose comparisons (e). Surface face-wise p-values showed in (e) are corrected for 10000 permutations, and the overall p-value is < 0.0001.

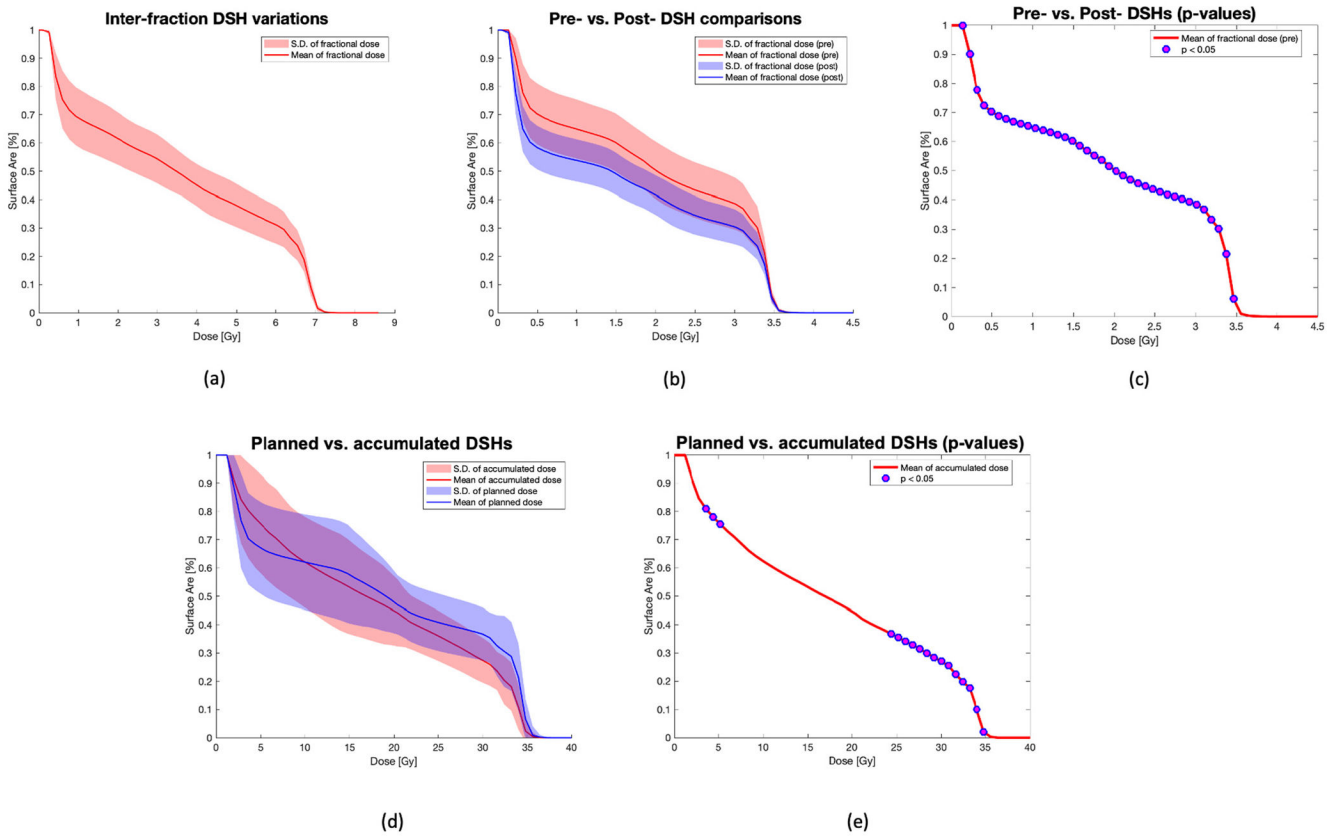

Figure 5:

DSH representations of inter-fraction variations (a), the mean and standard deviation of low (pre-RT) and high (post-RT) filling statuses (b), the bin-wise group comparisons of the low vs. the high filling status (c), as well as the mean and the standard deviation of the planned and the daily accumulated dose (d) and the bin-wise group comparison between the two groups (e). Blue circles denote significant bin-wise differences ($p<0.05$) in (c) and (e) that are corrected for 10000 permutations, and their overall p-value after the permutations are < 0.0001 and 0.0112, respectively.

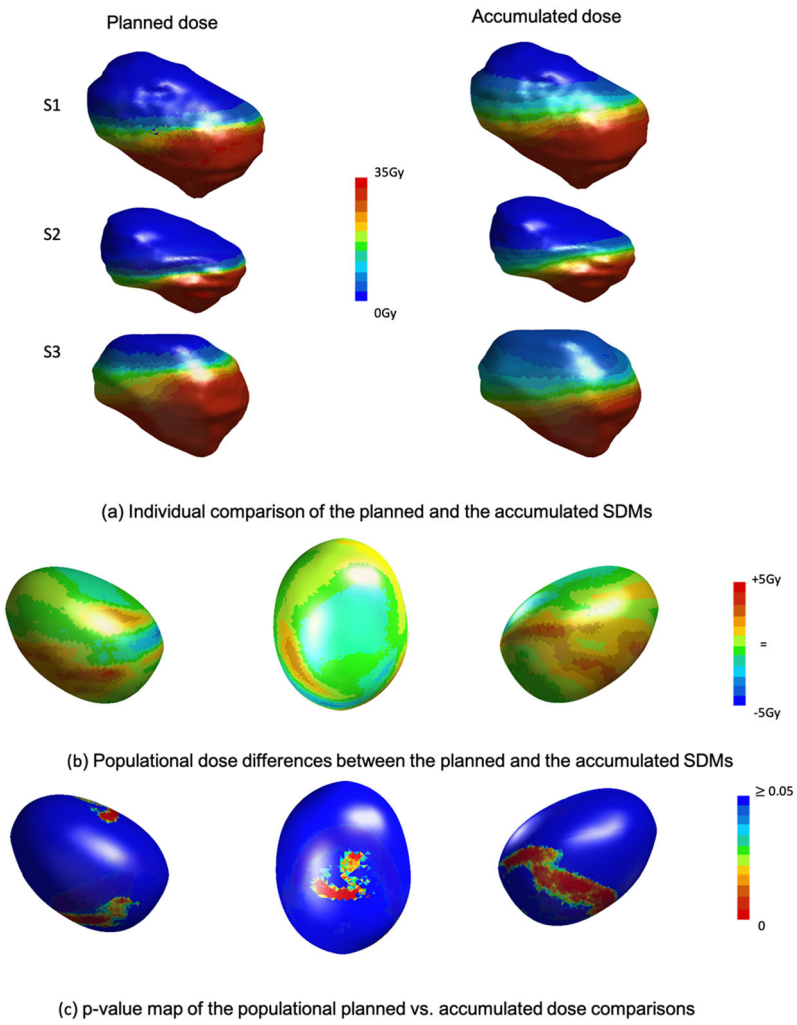

Figure 6:

Illustration of surface distributions of the planned vs. accumulated doses. From top to bottom are the planned and accumulated SDMs for three example patients (a), the populational averaged dose difference between the planned vs. the daily cumulative model (b), and p-values of the planned vs. the accumulated dose comparisons (c). Surface face-wise p-values showed in (c) are corrected for 10000 permutations, and the overall p-value is 0.0800.

Table 1:

A comparison between D_rigid and D_surf using three manually defined landmarks: Left and right ureters, as well as urethral orifice.

Landmarks	***Ureter L***	***Ureter R***	***Urethral Ori***
D_{rigid} (mm)	7.8 (±4.2)	8.7 (±3.7)	6.5 (±3.0)
D_{surf} (mm)	4.6 (±2.9)	4.8 (±3.2)	4.9 (±3.0)

Table 2:

P-value of statistical analyses on 7 pose parameters: s, θ_x, θ_y, θ_z, t_x, t_y, and t_z. Both the original p-values and the permutation-corrected ones are provided, with the significant p-values ($p < 0.05$) marked by *.

Pose parameters	*P*	*P-corrected*
s	3.36e-15*	<0.0001*
θ_x	7.48e-07*	<0.0001*
θ_y	0.2855	0.2868
θ_z	0.2841	0.2833
t_x	0.0638	0.0656
t_y	6.19e-08*	<0.0001*
t_z	5.07e-11*	<0.0001*